

DRAFT

ROYAL HOLLOWAY UNIVERSITY OF LONDON

M.SC THESIS

STUDENT ID: 100920158

**Comparative Analysis of Simulations and
Experimental Outcomes: Slow Extraction Driven by
RF Transverse Excitation at the CERN Proton
Synchrotron**

Author:

Thomas BASS

Supervisor:

Professor Stephen GIBSON

June 21, 2023



Contents

1	Introduction	4
1.1	Motivation	6
1.1.1	Extraction Methods	6
1.1.2	Performing Slow Extraction	8
1.1.3	Simulating Slow Extraction	8
1.2	Challenges	9
2	Theory	10
2.1	Single-Particle Transverse Beam Dynamics	10
2.1.1	Coordinate System	10
2.1.2	Orbital Variable Space	11
2.1.3	Design orbit and Dipoles	12
2.1.4	Focussing and Multipoles	13
2.1.5	Single-Particle Oscillatory Motion	14
2.2	Multi-Particle Transverse Beam Dynamics	17
2.2.1	Phase Space	17
2.2.2	Dispersion	18
2.2.3	Matrix Formalism	18
2.2.4	Normalised Phase Space	19
2.3	Multi-particle Longitudinal Dynamics	19
2.3.1	Magnetic Ramping	20
2.3.2	RF Ramping	21
2.3.3	Dispersion	21
2.3.4	Longitudinal Phase Space	23
2.4	Slow Extraction	23

3	Simulation and Benchmarking	24
3.1	Simulation Methodology	24
4	Conclusion	25
5	Acknowledgements	26
6	Bibliography	27
A	Derivations	31
A.1	Relating longitudinal variables	31
B	Code Snippets	32
C	Data and Plots	33

ABSTRACT

Resonant slow extraction is a beam extraction method which provides a continuous spill over a longer duration than can be achieved with fast single-turn or non-resonant multi-turn extraction. By using transverse excitation to drive the circulating particles onto the resonance, long-duration spills can be produced, and delivered to facilities such as fixed-target experiments, or hadron therapy gantries.

In order to accurately and efficiently simulate the extraction process over a wide range of timescales, new modelling tools and computing platforms must be explored. By utilising optimised computational hardware—such as General Purpose Graphics Processing Units (GPGPUs), and next-generation simulation software (such as Xsuite), computation times for simulations can be reduced by several orders of magnitude.

This thesis presents recent developments of resonant slow extraction modelling and benchmarking with a comparison to measurements made at CERN’s Proton Synchrotron (PS), with a particular focus on understanding the dynamics of transverse RF excitation and effect on spill quality.

Keywords Beam Physics, Slow Extraction, Radio-Frequency Knockout, Simulation, Xsuite

Chapter 1

Introduction

The CERN Proton Synchrotron (PS), alongside providing intermediary acceleration for hadron and ion beams for the Super Proton Synchrotron (SPS) and eventually the Large Hadron Collider (LHC), provides beams for the many fixed target experiments located at the East Area (EA) experimental facility. This facility, as illustrated in Figure 1.1, consists of the proton (IRRAD) and mixed-field (CHARM) irradiation facilities, via a dedicated 24 GeV/c beamline, in addition to a multi-target beamline providing three secondary beams.

Ongoing experiments in these facilities such as the CHARM High-energy Ions for Micro Electronics Reliability Assurance (CHIMERA) [1] use high-Z ions (Pb) to simulate the harsh radiation environment of cosmic rays which satellites experience. Using low-intensity ($<10^6$ ions/spill), high-energy (>100 MeV/u) beams, customers such as the European Space Agency can assess the reliability of new materials in these environments. Figure 1.2 illustrates the two injection chains of the PS, either with Lead ions sourced from the Linear Accelerator 3 (Linac3) and Low Energy Ion Ring (LEIR) chain, or protons from the Linac4 and the Proton Synchrotron Booster (PSB).

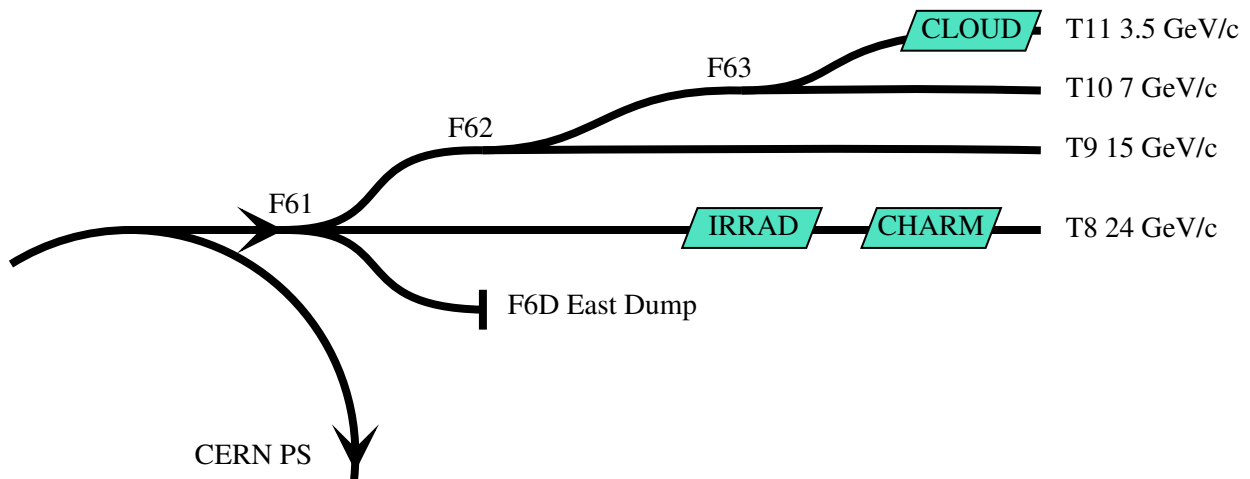


Figure 1.1: Layout diagram of the CERN East Area (EA) beamlines, their energies, and experiments.

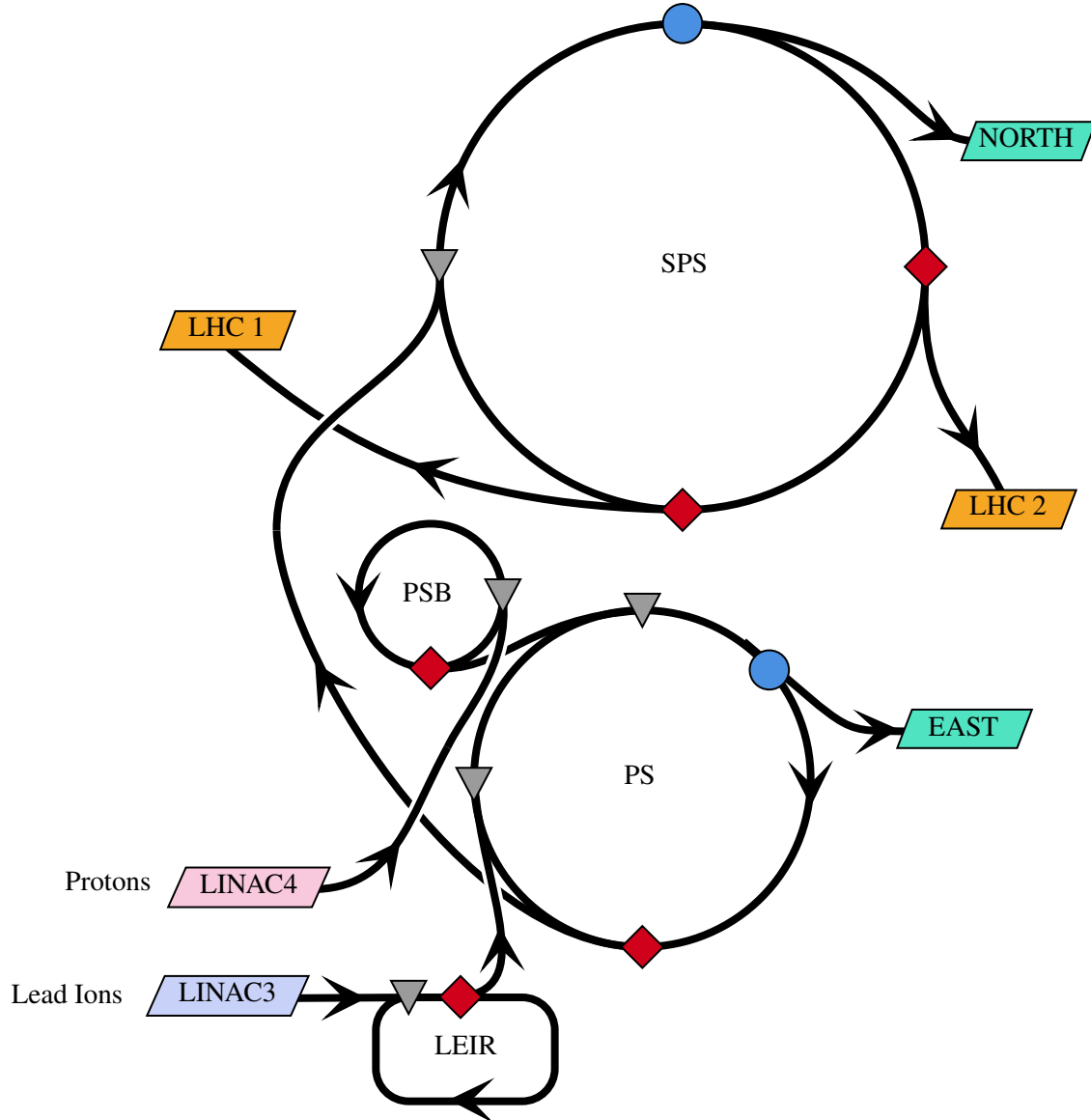


Figure 1.2: Layout diagram of the primary injection chain at CERN. Particles are sourced from either Linac 3 (for Lead ions) or Linac 4 (for Protons), and accelerated through the LEIR or PSB respectively. After injection and acceleration in the PS, beams are extracted either to the SPS or East Area (EA). Particles at the SPS are either extracted at two LHC extraction locations, or towards the North area. Red diamonds mark Fast extraction locations, and blue circles mark Slow extraction regions. Grey triangles mark injection regions.

1.1 Motivation

The CHIMERA experiment, and other experiments located at the East Area and its higher-energy sister site at the SPS North Area, are referred to as fixed-target experiments. These experiments require a semi-continuous flux of particles: if the entire beam of the PS was delivered to a material sample, for example, in an effectively instantaneous “spill” (a controlled removal of particles from the circular accelerator), any sensitive acquisition equipment would become saturated, and the fixed target itself likely destroyed.

At a beam momentum of 5.4 GeV in the PS, the revolution of the beam is around 470 kHz. Therefore, delivering particles over the period of one turn could, at most, provide a spill time on the order of 2 μ s. This extraction method, known as *fast* extraction, is commonly used to transfer particles between successive accelerators, where the bunched time-structure of the beam must be preserved. To provide spills on the order of ~ 100 ms required for these experiments, much longer than the revolution period, a “slow” extraction system is employed.

1.1.1 Extraction Methods

To move particles between consecutive machines along the primary CERN injector chain, the PSB, PS, and SPS are equipped with fast extraction systems. The principles of these processes will be fully explored in the next section, but a general overview and understanding of its benefits and disadvantages can help motivate the use of *slow* extraction.

As previously mentioned, *fast* extraction provides a spill of particles typically over the duration of one turn. A fast magnet, at a suitable location in the machine, imparts a large deflective force to the beam. This ejects the beam from the nominal orbit, where it encounters a second magnet—called a septum—to align the particle bunch along a transfer line. The opposite effect is then used to inject the bunch into the next machine: a magnet “kicks” the particles onto the circulating beam trajectory.

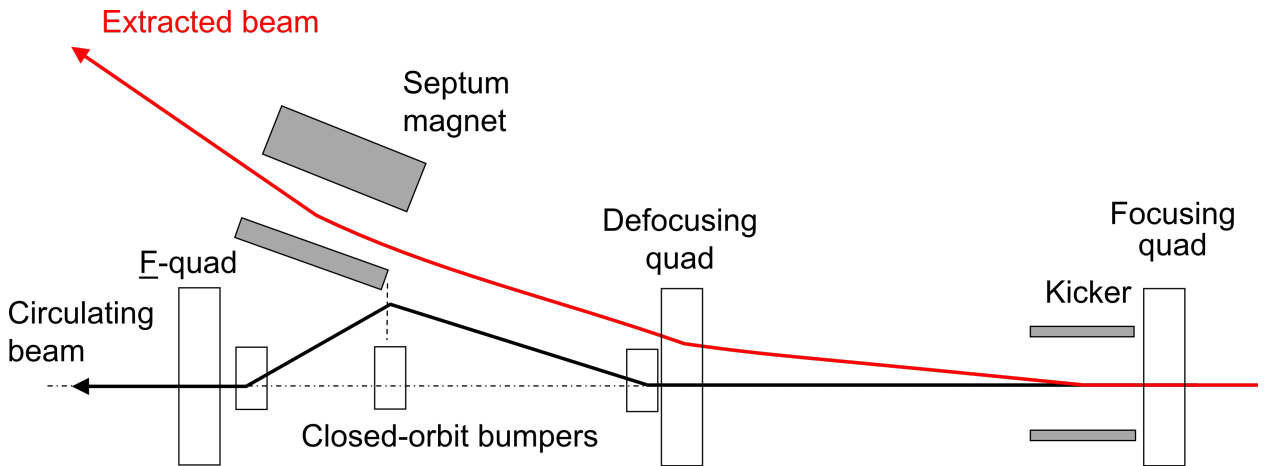


Figure 1.3: Diagram of a general single-turn fast extraction system. [2]

This general method of **single-turn fast extraction** (described in Figure 1.3) is performed at two locations in the SPS—Long Straight Sections (LSS) 4 and 6—to fill the two counter-rotating beamlines in the LHC [2]. The PSB performs similar extraction, but has the added complexity of “merging” four separate stacked accelerators to one transfer line [3]. LEIR likewise performs fast extraction [4]. The general layout of these

systems are shown in 1.2, where red diamonds mark fast extraction locations. Fast extraction systems are also used at the beam dump facilities at various stages of the accelerator chain.

In accelerator-to-accelerator contexts, the synchronous nature of fast extraction allows particles to remain bunched. **Multi-turn fast extraction** extends this benefit, and is performed when filling the SPS for its fixed-target experiments (North Area) from the PS. As the SPS (6.9 km) is almost approximately 11 times longer in circumference than the PS¹ (628 m), the entire SPS can be filled by 11 successive extractions of the full PS. This method, coined as *continuous transfer* (CT), introduces the concept of “shaving” the beam with an electrostatic septum. In its current implementation in the PS, the beam is bumped similarly to single-turn fast extraction, but is instead forced over the blade of an electrostatic septum (ES), such that a segment the beam is ‘sliced’ off, kicked towards a magnetic septum (MS), and extracted. The remaining beam is kicked back onto its orbit. The next turn, the beam has been “rotated” by a quarter turn, and the process repeats, until the finally the remaining core of the beam is bumped directly to the magnetic septum. This provides a spill to the SPS of five bunches over five beam rotations from a single PS bunch.

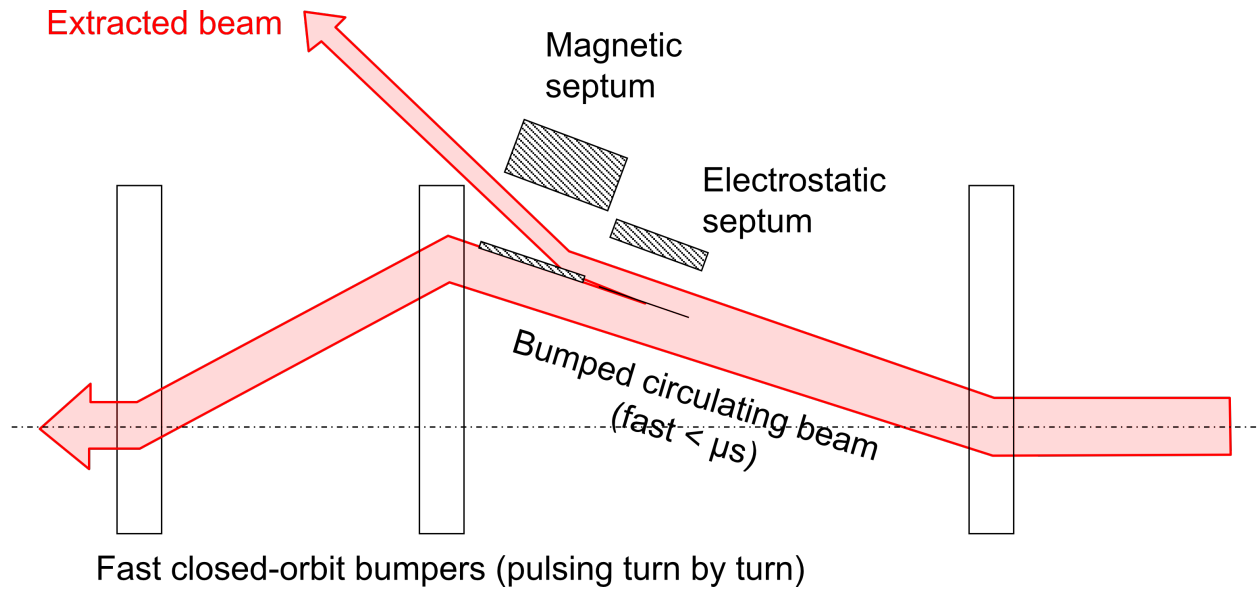


Figure 1.4: Diagram of a general multi-turn fast extraction system. [2]

This method of increasing the spill time is, however, limited by the width of the septum blades. As the amount of beam scraped off per turn decreases, the effect of the particles lost *on* the septum blade increases. To maintain a reasonable extraction efficiency, the beam size would have to become exponentially large.

For example, if a 50% extraction efficiency is desired over 10^4 turns, the beam thickness sliced off by the ES must be the same as the thickness of the blade itself. For the SPS, the ES has blade thickness of $25\text{ }\mu\text{m}$. The required diameter of the beam, therefore, would be $2 \cdot 25\text{ }\mu\text{m} \cdot 10^4 = 0.5\text{ m}$. This diameter is already larger than the beam pipes, clearly physically impossible.

In order to provide spills over a longer duration, approaching many thousands of turns, *slow extraction* must be used.

¹The PS is 100 meters across, and therefore $200\pi\text{ m}$

1.1.2 Performing Slow Extraction

Slow extraction (SX) instead relies on exploiting resonance of the beam as it oscillates around the orbit of the machine. A full theoretical description of these effects will be detailed in chapter 2, but a brief explanation is offered here: the oscillatory motion of a beam can be controlled such that it returns to the same point along the accelerators circumference with the same oscillation phase. The particles will, therefore, travel through the same field of a magnet, and experience the same force on consecutive turns. Akin to a child pushed on a swing in time with the peak of their oscillation, these particles will rapidly become unstable, the amplitude of their oscillations exponentially increasing.

This resonant effect is usually carefully avoided in particle accelerators. However, with the right configuration, this amplitude growth can be used instead of an ES to separate particles from their orbit, towards an MS, and into the extraction transfer line. Should the effect be slow enough, a tiny fraction of particles will reach the MS per turn, and with a large enough per-turn amplitude growth to reliably clear the blade thickness.

The exploitation of resonance to induce extraction is by no means novel; a method akin to slow extraction was first proposed by J. Tuck and L. Teng in 1951 [5], and performed by Le Couteur at the Liverpool cyclotron in 1954 [6]. Many such applications of slow extraction exist, using different effects to drive particles into resonance. This thesis will explore some of these methods, particularly focussing on Radio-Frequency Knockout slow extraction.

1.1.3 Simulating Slow Extraction

There are many applications for slow extraction systems beyond those currently used at CERN's experimental areas. Many medical synchrotrons, such as the MedAustron Synchrotron, use slow extraction to deliver beam to patients for ion beam cancer therapy [7]. Using the *Constant Optics Slow Extraction* (COSE) technique, spills of up to 30 s can be produced².

Obviously, in human medical applications, safety is extremely important. Therefore, the slow extraction process must be fully understood. Ripples in the intensity of beam have to be carefully controlled in order to provide a steady, predictable irradiation dose to patients.

Small medical synchrotrons are usually afforded the benefit of being simpler³, newer⁴, and having less demand for availability than larger research synchrotrons such as the PS. At such machines, extensive machine tests can be carried out to fully understand the extraction process. At CERN's PS, however, that benefit cannot be relied upon. Availability is in high demand, and studies are time-shared between machine development (MD), fixed-target experimental areas, LHC physics injection, and a wide array of other facilities.

Simulations can there provide a important tool in understanding slow extraction spills. New methods can be rapidly developed and tested without requiring extensive machine studies, and wide parameter spaces can be explored to construct functional relationships between input parameters and spill output characteristics.

²Limited to 10 s for patient treatment

³The PS contains 100 bending magnets along its circumference, as opposed to MedAustron's 16

⁴The PS began operation in 1959, and is CERN's oldest accelerator still in operation. MedAustron was first certified in 2016.

1.2 Challenges

Simulations for fast extraction are well understood; as explained later in chapter 2, the dynamics of particles in a “static”⁵ machine can be understood with simple matrix transformations. However, many slow extraction methods rely on dynamic machines—the aforementioned COSE technique, despite its name, is not performed on a static machine, but instead scales the strength of magnets with the change in particle momentum, creating *effectively* constant optics. Therefore, for each successive turn around the machine, the transport matrices must be re-calculated. For a typical slow extraction time of 500 ms at the PS, this equates to $\approx 235\,000$ turns, and orders of magnitudes more calculations.

There are long-standing, well-tested tools for computing these transfer matrices for particle accelerators, which describe the motion of a particle—or ensemble of particles—as it travels through the accelerator, encountering different magnetic and electric fields.

To aid with the design and construction of CERN’s Large Electron-Positron collider (LEP, the predecessor to LHC), the *Methodical Accelerator Design Program* (MAD) [8] was developed. This FORTRAN-based scripting tool allowed physicists to define the arrangement and strengths of magnetic elements around an accelerator (the *lattice*), define beam parameters and initial conditions, and calculate the resulting motion of particles (the *optics*). MAD, and its latest version, MAD-X, quickly became the *de facto* standard amongst particle accelerator institutions across the globe. However, in the twenty years since the release of MAD-X, the landscape of computational accelerator physics has become awash with a wide array of tools, codes, and standards, each with their own specialisations.

One particular improvement found in many new simulation programs is “ready-to-go” General-Purpose Graphical Processing Unit (GPGPU) acceleration. GPUs are specialised hardware capable of performing highly optimised matrix and vector calculations, initially intended for vector-based ray-tracing calculations. Where typical Central Processing Units have a wide range of general-purpose, unspecialised instructions and circuitry, GPUs are designed to perform a small set of highly optimised instructions on large arrays of data. This makes them ideal for the matrix calculations required for particle accelerator simulations. Additionally, where a typical CPU may contain anywhere from 4 to 64 cores, GPUs can contain many thousands of cores, capable of performing *embarrassingly parallel*⁶ calculations many orders of magnitude faster than a CPU.

⁵Static referring to the magnets and RF systems (known as the “optics” of the machine) being constant over the given time period.

⁶An *embarrassingly parallelisable* problem requires almost no effort to be separated into a large number of independent tasks which can be calculated concurrently.

Chapter 2

Theory

To construct accurate simulations of slow extraction methods, one must first understand the fundamental theory behind particle motion in a circular accelerator. This chapter will introduce the theory required to understand the motion of ensembles of particles as they travel through an accelerator, and how such oscillatory motion can be exploited to perform slow extraction. For a more in-depth treatment of beam dynamics and accelerator physics, the reader is referred to Wiedmann's *Introduction to Accelerator Physics* [9].

2.1 Single-Particle Transverse Beam Dynamics

2.1.1 Coordinate System

The coordinate systems used to describe the dynamic motion of particles in a particle accelerator such as the PS relies on the periodic nature of a circular accelerator. Using a traditional Cartesian x, y, z coordinate system would quickly introduce complications when describing circular trajectories, and so a local curvilinear coordinate system is used.

The basis vectors for this system, $(\hat{x}, \hat{y}, \hat{s})$, constantly rotate in Cartesian space as the reference particle moves along the orbit of the accelerator. The longitudinal vector \hat{s} is tangent to the particle's orbit, and the \hat{x} direction is parallel to the radius of the accelerator. The absolute direction of \hat{y} does not change, but makes one complete rotation in one closed orbit of the reference particle through the accelerator. This system is shown in Figure 2.1, along with the radius of the circular trajectory ρ , and the angle from the origin $s = 0$.

This coordinate system is academically known as a *Frenet-Serret* type coordinate system, and can be rigorously defined by the unit vector *tangent* to the curve \hat{T} (pointing in the direction of motion), the unit vector *normal* to the tangent and on the tangential plane \hat{N} , and the binormal unit vector \hat{B} , the cross product of \hat{T} and \hat{N} . These unit vectors, forming an orthonormal basis spanning \mathbb{R}^3 , and known collectively as the **TNB** frame, are equal to the vectors $\hat{x}, \hat{y}, \hat{s}$ by:

$$\begin{pmatrix} \hat{T} \\ \hat{N} \\ \hat{B} \end{pmatrix} = \begin{pmatrix} \hat{s} \\ -\hat{x} \\ \hat{y} \end{pmatrix} \quad \text{Eq. 2.1}$$

The coordinate system $(\hat{x}, \hat{y}, \hat{s})$ relies on the right-hand chirality (Figure 2.2) of the vector cross product for the \hat{x} vector to point radially outwards from the centre of the machine, the \hat{y} vector points upwards,

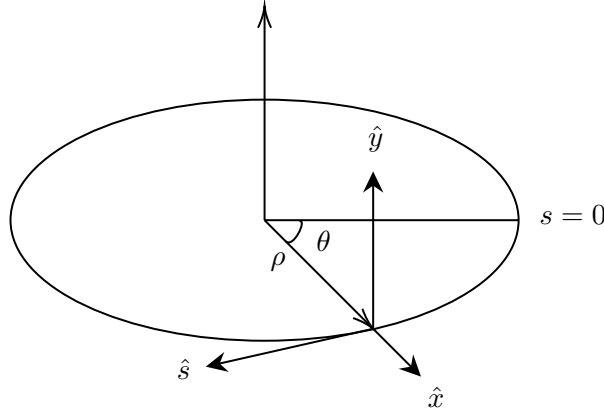


Figure 2.1: The *Frenet-Serret* vectors used to define the coordinate system used in particle beam dynamics.

and the \hat{s} vector points in the direction of motion. The direction of \hat{x} to point outwards from the centre of revolution is chosen as injection and extraction line apertures will therefore be located in the positive \hat{x} .

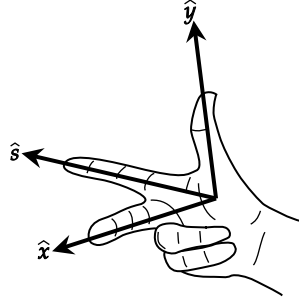


Figure 2.2: The right-hand chirality rule defining the direction of $\hat{x} = \hat{y} \times \hat{s}$

2.1.2 Orbital Variable Space

Following the basis vectors defining the coordinate system, the following variables are used to characterise the orbit of particles, dependent on s :

- $x(s)$ [m] — the particle's horizontal position with respect to the reference orbit.
- $y(s)$ [m] — the particle's vertical position with respect to the reference orbit.
- $t(s) = -c\Delta t$ [m] — the particle's arrival delay with respect to the reference orbit, multiplied by the speed of light c .
- $x'(s) = \frac{dx}{ds}$ [rad] — the particle's horizontal angle with respect to the reference orbit.
- $y'(s) = \frac{dy}{ds}$ [rad] — the particle's vertical angle with respect to the reference orbit.
- $p_t(s) = \Delta E/pc$ — the particle's energy difference, divided by the reference momentum times the speed of light c .

These variables provide a 6-tuple fully describing the trajectory of a particle. However, for the remainder of this thesis, the pair longitudinal variables t, p_t will be treated separately to the transverse variable pairs (x, x') and (y, y') . This enables a simpler understanding of the effects of beam bending and focussing

magnets, as these effects are independent of the longitudinal variables. Conversely, longitudinal beam dynamics requires understanding of RF devices.

2.1.3 Design orbit and Dipoles

All descriptions of particle accelerators are built upon the Lorentz force, describing the force \vec{F} acting on a charged particle with charge q as it moves through an electric field \vec{E} and magnetic field \vec{B} with velocity \vec{v} , given as

$$\vec{F}_{\text{lorentz}} = q \cdot (\vec{E} + \vec{v} \times \vec{B}) \quad \text{Eq. 2.2}$$

This equation can already show why magnetic fields are used in almost all areas of particle acceleration, and not electric fields; a particle with higher velocity v will experience a greater force from a constant magnetic field \vec{B} , whereas the contribution from the electric field \vec{E} will remain constant. Therefore, at velocities approaching the speed of light ($v \rightarrow c$), we can begin to neglect \vec{E} for some derivations.

The other force experienced by a particle in an accelerator is the centripetal¹ force:

$$\vec{F}_{\text{centrif.}} = \frac{m_0 v^2}{\rho} \quad \text{Eq. 2.3}$$

where m_0 is the particle's rest mass, and ρ is the radius of the particle's orbit inside the accelerator.

Equating equations 2.3 and 2.2 yields

$$B\rho = \frac{p}{q} \quad \text{Eq. 2.4}$$

The quantity $B\rho$ is known as the *momentum rigidity* of a beam, and defines the bending angle of a particle for a given magnetic field.

If the momentum $p = mv$ of the particle is measured in GeV/ c_0 /amu, and A and Z are the atomic mass number and charge of the particle, the momentum rigidity can be expressed in Tesla-meters:

$$B\rho \text{ [T m]} = \frac{p}{q} = \frac{A}{Z} \times 3.33564 \times q \text{ [GeV}/(c_0 \text{ u})] \quad \text{Eq. 2.5}$$

However, this formulation only describes a single magnetic field. In order to bend the particles along a circular trajectory, dipole magnets are used to create near-constant fields through which the particles travel. Again referring to Equation 2.2 (with the help of Figure 2.2), a magnetic field pointed vertically upwards (along the \hat{y} vector) will cause a particle with motion along the \hat{s} vector to experience a bending force along the $-\hat{x}$ direction (illustrated in Figure 2.3).

The arrangements of these bending magnets—referred to as Main Units (MU)—will define the closed loop of one orbit in the accelerator—the *design orbit*.

If α is the bending angle of a single MU, then α can be related to the momentum rigidity by

$$\alpha = \frac{ds}{\rho} = \frac{B ds}{B\rho} \quad \text{Eq. 2.6}$$

¹While the coordinate system used allows for a reference frame whose orientation follows the orbit, this frame is not co-moving with the particles, but still fixed in the “laboratory” frame—otherwise, complex Lorentz transformations would be required.

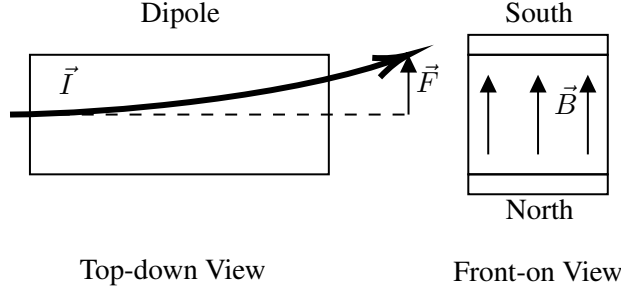


Figure 2.3: A dipole magnet, showing the direction of the magnetic field, \vec{B} , the current of the particle, \vec{I} , and the force, \vec{F} , on a positively charged particle.

Integrating this over all magnets in the ring, therefore, must be equal to one full revolution, 2π

$$\frac{\int B ds}{B\rho} \equiv 2\pi \quad \text{Eq. 2.7}$$

This provides one of the first key insights which is not obvious at first—that “circular” accelerators are in fact n-sided polygons, with bending magnets at each vertex, and a *drift* (accelerator sections without any significant electromagnetic field) or other non-bending multipole magnet at each side: in the case of the LHC, 1,232 dipole magnets are used to keep the beam on it’s circular path; in the PS—100.

2.1.4 Focussing and Multipoles

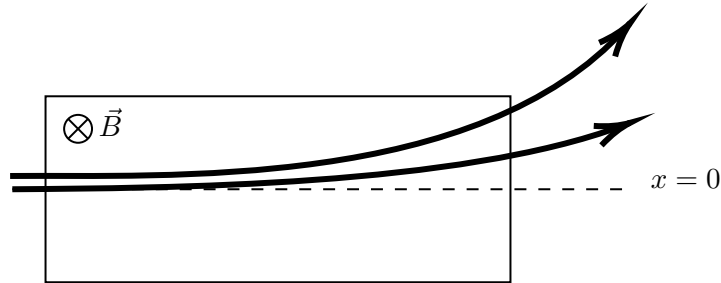


Figure 2.4: A top-down diagram of a dipole illustrating how small changes in the beam’s position, x , are amplified by the bending effect of the magnet.

Figure 2.4 illustrates the need for corrective elements in the beamline. If a particle is displaced slightly from the design orbit ($x = 0$) before a dipole element (marked with a downwards magnetic field \vec{B}), the bending effect will be greater, and the particle will be displaced further from the design orbit after the dipole.

To correct for this, synchrotrons use quadrupole elements to “focus” the beam in one transverse plane. An arrangement of four magnetic poles creates a field stronger at higher $|x|$ displacement, causing particles to be pulled back towards the design orbit. However, particles off-axis in the other transverse plane will be pushed further off-axis. To correct for this, a second quadrupole is placed further along in the beamline, with the magnetic poles arranged in the opposite orientation. This arrangement, known as a FODO lattice, is shown in Figure 2.5 (right).

Sextupoles—third order magnets—provide additional correction to the beam. Here, we can begin to expand on the optical analogy used thus far. Figure 2.6 shows a full arrangement of a dipole, sextupole, and focussing quadrupole. In the optical analogy, the Dipole takes the role of a prism, bending the light. As

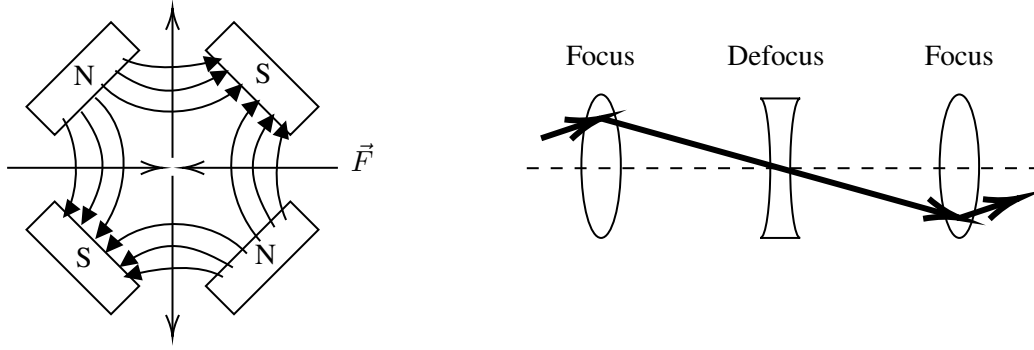


Figure 2.5: Diagram (left) showing the field of a *normal* oriented quadrupole, providing focussing in x but defocussing in y . Right-hand diagram illustrates a FODO cell.

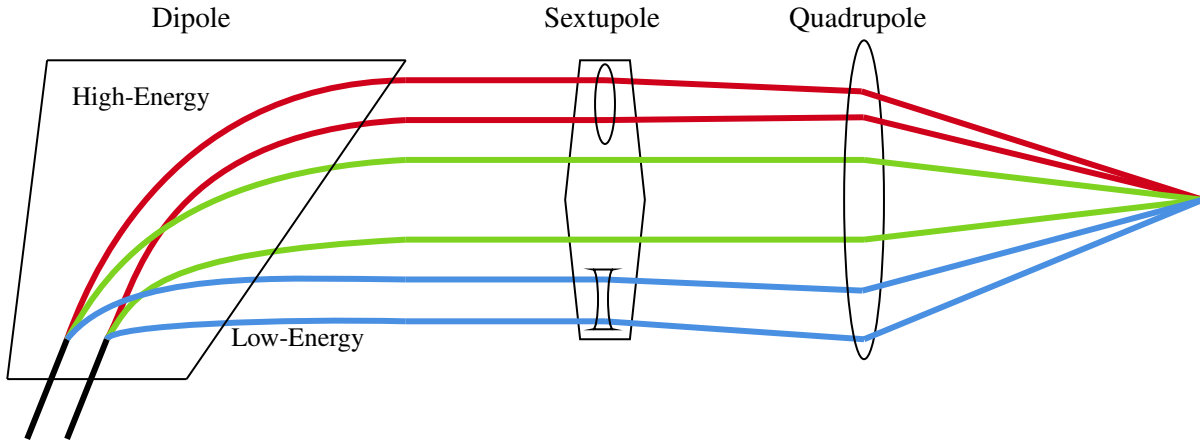


Figure 2.6: A diagram showing how Dipoles, Quadrupoles, and Sextupoles are used together to create the desired beam dynamics for particles with different energies.

with prisms, beams with higher energy are bent less than low energy, and so the component wavelengths (or energies) in the beam are dispersed. The sextupole is analogous to an aspherical element, correcting for chromatic aberration introduced by the focussing quadrupole. Again, as with its optical analogue—a focussing lens—the quadrupole has shorter focal length for higher energy particles. The sextupole acts as a focussing lens at high energy and diverging lens at low energy, correcting for this chromatic effect.

Now that the basic magnetic elements have been introduced, and an understanding of the beam's momentum p has been formed, we can redefine our transverse coordinates in terms of momentum: $p_x = x' \cdot p$ and $p_y = y' \cdot p$ now define our transverse coordinates. These coordinates will allow us to build a picture of the multi-particle transverse dynamics of the beam.

2.1.5 Single-Particle Oscillatory Motion

In a periodic (circular) accelerator, the linear equation for transverse motion takes the form of a differential equation:

$$x''(s) - x \cdot \left(k - \frac{1}{\rho^2} \right) = 0 \quad \text{Eq. 2.8}$$

where x is the transverse displacement as a function of longitudinal position s , and k is the quadrupole focussing coefficient, defined as

$$k = \frac{q}{p} \cdot \frac{dB_y}{dx} \quad \text{Eq. 2.9}$$

where q is the particle's charge, p is the longitudinal momentum, and B_y is the vertical component of the magnetic field. The $1/\rho^2$ term represents the effect of the dipole bending field, providing a weak focussing component. From here, it is clear that the transverse motion of particles, in a circular accelerator and under the influence of dipole focussing $1/\rho^2$ and quadrupole focussing k , follows a harmonic oscillator. If we enforce the periodicity² in s of k , Equation 2.8 can be rewritten in a compact form

$$x''(s) - \tilde{k}(s)x(s) = 0 \quad \text{Eq. 2.10}$$

where the quadrupole focussing component $\tilde{k}(s)$ is now a function of s .

This equation can be physically understood with another analogous example: one where the weak focussing effect of the dipoles are modelled as the curved sides of a toroidal, akin to a circular gutter pipe, illustrated in 2.7. The weak focussing effect creates harmonic motion for particles not on the ideal zero-amplitude path. This describes how the harmonic motion, described by Equation 2.10, relates to motion around an ideal orbit.

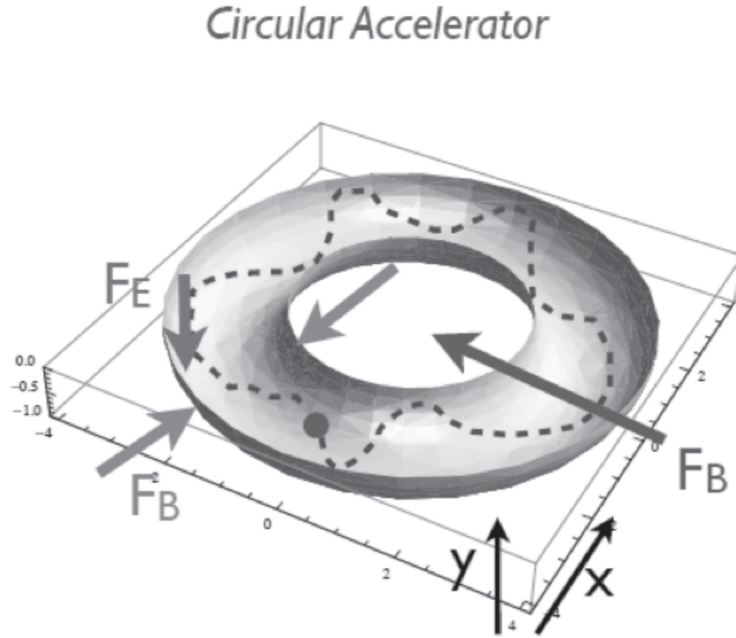


Figure 2.7: A diagram showing the analogy between the transverse motion of a particle in a circular accelerator and a ball rolling in a circular gutter.

With the given periodic boundary condition $\tilde{k}(s + L) = \tilde{k}(s)$, 2.10 is known as the Hill's equation.

Following Floquet's theorem [10], general solution to this equation takes the form of

$$x(s) = \sqrt{\varepsilon} \sqrt{\beta(s)} \cos(\varphi(s) - \varphi_0) \quad \text{Eq. 2.11}$$

²i.e. that the quadrupoles do not change between consecutive revolutions

where ε and φ_0 are integration constants characterising the initial conditions of the particle, and $\beta(s)$ and $\varphi(s)$ are the amplitude and phase functions (respectively) of the oscillation.

The β amplitude function must also satisfy the periodic constraint $\beta(s + L) = \beta(s)$, and can be related to the φ phase function by the following equation:

$$\varphi(s) = \int_0^s \frac{ds}{\beta(s)} \quad \text{Eq. 2.12}$$

Taking the derivative of Eq. 2.11 with respect to s gives an equation for the angle of the trajectory:

$$x'(s) = \sqrt{\varepsilon} \sqrt{\beta(s)} \left(\frac{1}{2} \beta'(s) \cos(\varphi(s) - \varphi_0) + \sin(\varphi(s)) \right) \quad \text{Eq. 2.13}$$

A basic analysis of Eq. 2.12 shows that at locations with large β amplitude (and thus a large transverse displacement), phase advance φ is small, and vice versa. The overall phase advance of transverse oscillations over one revolution of 2π is known as the *betatron tune* of the accelerator, and is defined as

$$Q = \frac{1}{2} \oint \frac{ds}{\beta(s)} \quad \text{Eq. 2.14}$$

This quantity, often simply referred to as *tune*, effectively indicates how many complete transverse oscillations a particle makes in one turn. The fractional part of this value is the most significant, and often a tune will be reference to the integer part; a tune of $Q = 6.\dot{3} = 19/3$ is, for the purposes of this thesis, equivalent to $Q = 1/3$.

2.2 Multi-Particle Transverse Beam Dynamics

2.2.1 Phase Space

Equation 2.11 and Equation 2.13 introduced an integration constant ε , which is a characteristic parameter of the particle or ensemble of particles. It is known as (transverse) emittance, and is usually considered with particle ensembles in mind. These two equations can be manipulated to provide an expression for ε :

$$\varepsilon = \gamma(s)x^2(s) + 2\alpha x(s)x'(s) + \beta(s)x'^2(s) \quad \text{Eq. 2.15}$$

where

$$\alpha(s) = -\frac{1}{2} \frac{d\beta(s)}{ds} \quad \text{Eq. 2.16}$$

and

$$\gamma(s) = \frac{1 + \alpha^2(s)}{\beta(s)} \quad \text{Eq. 2.17}$$

These further two constants, along with β , form the *Courant-Snyder Parameters* [11], commonly referred to as the *twiss* parameters³.

These parameters can be readily understood in the *phase space*⁴ of (x, x') . Illustrated in Figure 2.8, Equation 2.15 describes an ellipse, which covers the area of the particle ensemble in phase space. The area of this ellipse is given by $\pi \cdot \varepsilon$, and may be interchangeably defined as the emittance.

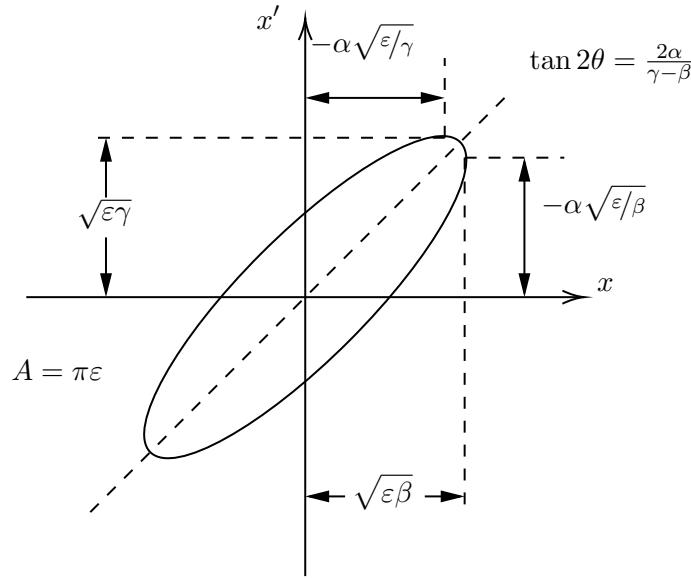


Figure 2.8: Phase space in (x, x') showing the ellipse formed by a particle, and its relation to the Twiss parameters.

Liouville's theorem states that, under conservative forces, this emittance is conserved, and no external field can change it, and hence Equation 2.11 provides it as an invariant of motion.

³Even Richard Q. Twiss, a British astronomer, was himself unsure as to how the parameters became attributed to him [12].

⁴This is opposed to the more formal phase space (x, p_x) , which does not provide these insights as succinctly.

2.2.2 Dispersion

We now consider the oscillatory motion of *multiple* particles, with reference to the ideal particle. This ideal particle, with momentum p_0 and initial conditions all equating to zero, has a path through the field centre of all quadrupoles, and so experiences no quadrupole effect k . This means that its motion is controlled by the weak dipole focussing $1/\rho^2$. A nominal particle, still with momentum p_0 but with initial displacement and/or angle conditions, will perform closed-loop betatron oscillations around this path.

A particle with a momentum offset, $\Delta p = p - p_0 > 0$, will still satisfy 2.8 from before, but the inhomogeneous form

$$x''(s) - x \left(k - \frac{1}{\rho^2} \right) = \frac{1}{\rho} \frac{\Delta p}{p_0} \quad \text{Eq. 2.18}$$

We can use the homogenous solution previously found to form the complete solution $x(s) = x_h(s) + x_i(s)$. This inhomogeneous term $x_i(s)$, is normalised by the momentum difference to produce the Dispersion function

$$D(s) = \frac{x_i(s)}{\Delta p/p_0} \quad \text{Eq. 2.19}$$

describing how the additional amplitude of an off-momentum particle depends on the momentum difference. This dispersion function satisfies, for the circumference of the machine:

$$D'' - D \left(x - \frac{1}{\rho^2} \right) = \frac{1}{\rho(s)} \quad \text{Eq. 2.20}$$

2.2.3 Matrix Formalism

Outside of the context of periodic boundary conditions, Equation 2.11 and Equation 2.13 can be solved by imposing initial conditions x_0 and x'_0 :

$$x(s) = x_0 \cos(\sqrt{K} \cdot s) + \frac{x'_0}{\sqrt{K}} \sin(\sqrt{K} \cdot s) \quad \text{Eq. 2.21}$$

$$x'(s) = -x_0 \sqrt{K} \sin(\sqrt{K} \cdot s) + x'_0 \cos(\sqrt{K} \cdot s) \quad \text{Eq. 2.22}$$

where K now defines the quadrupole focussing effect k (Equation 2.9) and the dipole weak focussing effect:

$$K = \frac{1}{\rho^2} - k \quad \text{Eq. 2.23}$$

These two equations can be combined into a matrix equation:

$$\begin{pmatrix} x \\ x' \end{pmatrix} = \mathbf{M} \begin{pmatrix} x_0 \\ x'_0 \end{pmatrix} \quad \text{Eq. 2.24}$$

where \mathbf{M} is the transfer matrix

$$\mathbf{M} = \begin{pmatrix} \cos(\sqrt{K} \cdot s) & \frac{1}{\sqrt{K}} \sin(\sqrt{K} \cdot s) \\ -\sqrt{K} \sin(\sqrt{K} \cdot s) & \cos(\sqrt{K} \cdot s) \end{pmatrix} \quad \text{Eq. 2.25}$$

The definition of this transfer matrix \mathbf{M} can be expanded to define the variety of magnets used in an accelerator. In the simple case, where no magnet is present, we define the transfer matrix for a drift space of

length L :

$$\mathbf{M}_{\text{drift},x} = \mathbf{M}_{\text{drift},y} = \begin{pmatrix} 1 & L \\ 0 & 1 \end{pmatrix} \quad \text{Eq. 2.26}$$

For a normal dipole magnet bending only horizontally, where $k = 0$ and $K_x = 1/\rho^2$, the transfer matrix is:

$$\mathbf{M}_{\text{dipole},x} = \begin{pmatrix} \cos\left(\frac{L}{\rho}\right) & \rho \sin\left(\frac{L}{\rho}\right) \\ -\frac{\sin\left(\frac{L}{\rho}\right)}{\rho} & \cos\left(\frac{L}{\rho}\right) \end{pmatrix} \quad \text{Eq. 2.27}$$

$$\mathbf{M}_{\text{dipole},y} = \mathbf{M}_{\text{drift},y} \quad \text{Eq. 2.28}$$

For a normal quadrupole, where $K_x = -k$ and $K_y = k$, the transfer matrix is:

$$\mathbf{M}_{\text{quad},x} = \begin{pmatrix} \cos(\sqrt{-k} \cdot L) & \frac{1}{\sqrt{-k}} \sin(\sqrt{-k} \cdot L) \\ -\sqrt{-k} \sin(\sqrt{-k} \cdot L) & \cos(\sqrt{-k} \cdot L) \end{pmatrix} \quad \text{Eq. 2.29}$$

$$\mathbf{M}_{\text{quad},y} = \begin{pmatrix} \cos(\sqrt{k} \cdot L) & \frac{1}{\sqrt{k}} \sin(\sqrt{k} \cdot L) \\ -\sqrt{k} \sin(\sqrt{k} \cdot L) & \cos(\sqrt{k} \cdot L) \end{pmatrix} \quad \text{Eq. 2.30}$$

If we define the properties of each element in the accelerator (the lattice), we can then define the transfer matrix for the entire accelerator as the product of the transfer matrices of each element. For example, a FODO lattice with an initial bending dipole can be defined as:

$$\mathbf{M}_{\text{total}} = \mathbf{M}_{\text{dipole}} + \mathbf{M}_{\text{quad}} + \mathbf{M}_{\text{drift}} - \mathbf{M}_{\text{quad}} + \mathbf{M}_{\text{drift}} + \dots \quad \text{Eq. 2.31}$$

This is the principle by which *particle tracking codes*, such as MAD-X, operate. An input lattice file defines the structure and properties of the magnets composing the accelerator, and particle variables are then computed with matrix multiplication.

2.2.4 Normalised Phase Space

Expanding on the idea of matrix formalism and the phase space ellipse, many particle tracking codes operate in *normalised* phase space (x_n, x'_n) —that is, where the phase space of (x, x') is linearly transformed in a way which results in the phase space ellipse becoming circular. The matrix transformation is therefore defined as

$$\begin{pmatrix} x \\ x' \end{pmatrix} = \begin{pmatrix} \frac{1}{\sqrt{\beta_x}} & 0 \\ \frac{\alpha_x}{\sqrt{\beta_x}} & \sqrt{\beta_x} \end{pmatrix} \begin{pmatrix} x_n \\ x'_n \end{pmatrix} \quad \text{Eq. 2.32}$$

2.3 Multi-particle Longitudinal Dynamics

We will complete the initial picture of accelerator dynamics by considering the longitudinal dynamics of a beam. This is largely understood separately from the transverse motion, but with similar concepts.

Where the transverse planes principally consider bending and focussing effects from magnetic fields, the longitudinal plane considers acceleration effects from standing RF fields. RF cavities are engineered to create a steady-state field at the cavity's resonance. This resonant frequency defines the RF structure of the

device—the SPS, for example, employs 200 MHz RF system for acceleration, and a 800 MHz system for beam stabilisation [13], where the PS similarly uses a 10 MHz system [14].

Returning again to Equation 2.2, we instead now neglect the *magnetic* component; this term is always perpendicular to the direction of motion, so has no acceleration component. This equation can then be used with the potential of the electric field. From Equation 2.2:

$$\vec{F} = q\vec{E} = \frac{dp}{dt} \quad \text{Eq. 2.33}$$

where, again, q is the charge of the particle, and \vec{E} is the electric field. Using the relativistic formula

$$E^2 = E_0^2 + p^2 c^2 \quad \text{Eq. 2.34}$$

and taking its derivative, we obtain

$$2E dE = 2pc^2 dp \Rightarrow dE = \frac{c^2 mv}{E} dp = v dp \quad \text{Eq. 2.35}$$

Taking the derivative again, along the longitudinal axis s :

$$\frac{dE}{ds} = v \frac{dp}{ds} = \frac{dp}{dt} = qE_s \quad \text{Eq. 2.36}$$

This defines the kinetic energy W gained along the s axis as

$$W = q \int E_s ds = qV \quad \text{Eq. 2.37}$$

where V is the electric field potential.

An electric field of magnitude E_0 travelling in the s direction can be defined as

$$E_s = E_0 \cos(\omega_{RF}t - ks) \quad \text{Eq. 2.38}$$

where ω_{RF} is the RF frequency, related to the wave number k by $k = \omega_{RF}/v_\phi$, where v_ϕ is the phase velocity of the wave. In a synchrotron, where the orbit of particles is of constant radius, the magnetic field B needs to increase in time (*ramp*) as the particle is accelerated. Additionally, to keep the particle in phase with the RF cavity, the frequency of the RF ω_{RF} must increase as the particle gains energy. This synchronous condition, for velocities $v \ll c$, is defined as

$$\frac{2\pi\rho}{v_s} = \frac{h}{\omega_{RF}} \quad \text{Eq. 2.39}$$

where h is the RF harmonic, the number of RF cycles per revolution. For East Area beams in the PS, $h = 8$ acceleration is used. This means that there are eight stable “particles”, spread equidistantly around the ring circumference.

2.3.1 Magnetic Ramping

To keep a particle with increasing energy bent along a path of constant radius, the magnetic field B of the bending dipoles must increase as RF acceleration occurs. Recalling Equation 2.4, and deriving by time, obtains

$$\frac{dp}{dt} = q\rho\dot{B} \quad \text{Eq. 2.40}$$

For one turn in a synchrotron, this results in a momentum gain

$$\Delta p_{rev} = q\rho \dot{B} T_{rev} = \frac{Lq\rho R\dot{B}}{v} \quad \text{Eq. 2.41}$$

where L is the machine length. Recalling Equation 2.34, $\Delta E = v\Delta p$, and so the energy gain per revolution is

$$\Delta E_{rev} = Lq\rho R\dot{B} = qV \sin \phi_s \quad \text{Eq. 2.42}$$

where ϕ_s is the synchronous phase. This stable phase therefore changes while energy is ramped:

$$\phi_s = \arcsin \left(L\rho \frac{\dot{B}}{V_{RF}} \right) \quad \text{Eq. 2.43}$$

2.3.2 RF Ramping

The RF frequency must also ramp as particles increase in energy, and revolution frequency increases. From the earlier definition $\omega_{RF} = \omega h$:

$$\frac{f_{RF}}{h} = f_{rev} = \frac{v}{2\pi R} = \frac{1}{2\pi} \frac{qc^2}{E} \frac{\rho}{R} B \quad \text{Eq. 2.44}$$

2.3.3 Dispersion

Next, akin to subsection 2.2.2, we consider small perturbations in momentum with respect to an ideal path. We define two parameters:

$$\alpha_p = \frac{\Delta L/L}{\Delta p/p} \quad \text{Eq. 2.45}$$

where α_p , the *momentum compaction factor*, is distinct from the relativistic α_c and Twiss parameter α .

$$\eta = \frac{\Delta f_{rev}/f_{rev}}{\Delta p/p} \quad \text{Eq. 2.46}$$

where η , the *slip factor*, is the relative change of revolution frequency with momentum.

Using the dispersion function Equation 2.19, we can relate the momentum compaction factor to its effect on orbit length s_0 [15, 5.1]

$$\alpha_c = \frac{1}{L} \int \frac{D_x(s)}{\rho(s)} ds_0 \quad \text{Eq. 2.47}$$

Using the revolution frequency⁵ $f_{rev} = \beta_c c / 2\pi R$, we define the relative revolution frequency change Δf_{rev} as

$$\Delta f_{rev} = \frac{d\beta_c}{\beta_c} - \frac{dR}{R} = \frac{d\beta_c}{\beta_c} - \alpha_c \frac{dp}{p} \quad \text{Eq. 2.48}$$

We recall the gamma Lorentz factor $\gamma_c = 1/\sqrt{1 - \beta_c^2}$, and, via $p = mv$ obtain

$$p = mv = \frac{E_0}{c} \beta_c \gamma_c \quad \text{Eq. 2.49}$$

$$\frac{dp}{p} = \frac{d\beta_c}{\beta_c} + \frac{d(1 - \beta_c^2)^{-1/2}}{(1 - \beta_c^2)^{-1/2}} = \gamma_c \frac{d\beta_c}{\beta_c} \quad \text{Eq. 2.50}$$

⁵NB: β_c here refers to the relativistic Lorentz factor v/c

Therefore, the relative change in frequency can also be defined as

$$\frac{\Delta f_{rev}}{f_{rev}} = \left(\frac{1}{\gamma_c^2} - \alpha_c \right) \frac{\Delta p}{p} \quad \text{Eq. 2.51}$$

and so the slip factor can be defined in terms of α_c and γ_c as

$$\eta = \frac{1}{\gamma_c^2} - \alpha_c \quad \text{Eq. 2.52}$$

This defines a *transition energy* γ_{tr} such that $\eta = 0$, causing no change in revolution frequency f_{rev} for a small momentum change Δp :

$$\gamma_{tr} = \frac{1}{\sqrt{\alpha_c}} \quad \text{Eq. 2.53}$$

Above this transition energy, where $\eta < 0$, the particle has velocity $v \rightarrow c$, and so the path-length change dominates the velocity change. This is the standard configuration of accelerators. Below this transition energy, where $\eta > 0$, the increase of velocity is significantly larger than the path-length change effect. At this transition energy, both effects compensate, and so f_{rev} becomes independent of Δp . Here, the *synchrotron* longitudinal oscillations stop, and particles not on the synchronous phase ϕ_s will rapidly gain energy, and become lost due to dispersion D .

The effect of crossing the transition energy can be visualised with the typical electric field oscillator from Equation 2.42. Shown in Figure 2.9, the energy gain of a particle is plotted as a function of its phase ϕ . The synchronous phase, ϕ_s (Equation 2.43), is found on the “falling” edge of the sin RF signal; a particle which arrives too “early” ($\phi < \phi_s$) will receive a *higher* energy gain than the synchronous particle ϕ_s , and so its revolution time will increase due to the dominant effect of path length. On the next turn, it will arrive slightly later, and gradually tend towards a phase of ϕ_s . Correspondingly, a “late” particle $\phi > \phi_s$ will receive less energy gain than ϕ_s , arrive earlier, and tend towards ϕ_s .

Below transition energy, $\eta > 0$, this effect is reversed, and the synchronous phase is stable on the rising RF slope.

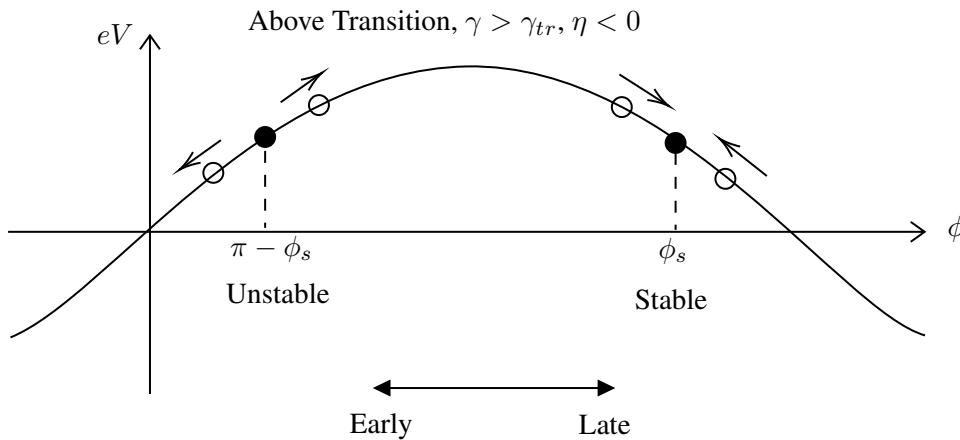


Figure 2.9: The energy gain of a particle in a standing wave cavity **above transition energy** as a function of phase. Above transition energy, longitudinal oscillations are stable on the *falling slope*. Four non-synchronous particles are shown, two stable around ϕ_s , and two unstable around $\pi - \phi_s$.

2.3.4 Longitudinal Phase Space

These effects can be analysed by, again, considering phase space coordinates—this time in the longitudinal plane. Again, akin to subsection 2.2.1, this space is constructed with variables $(\phi, \Delta p/p)$. A full derivation for the longitudinal motion invariants can be found in [15], but the effect of phase instability can be seen in Figure 2.9, where a phase greater than $\pi - \phi_s$ no longer provides the stabilising restoring force.

Outside of this stable envelope, demarcated by the *separatrix*, particles are lost to instability. The region within the separatrix is known as the *RF bucket*, and the area occupied by stable particles, the *RF emittance*.

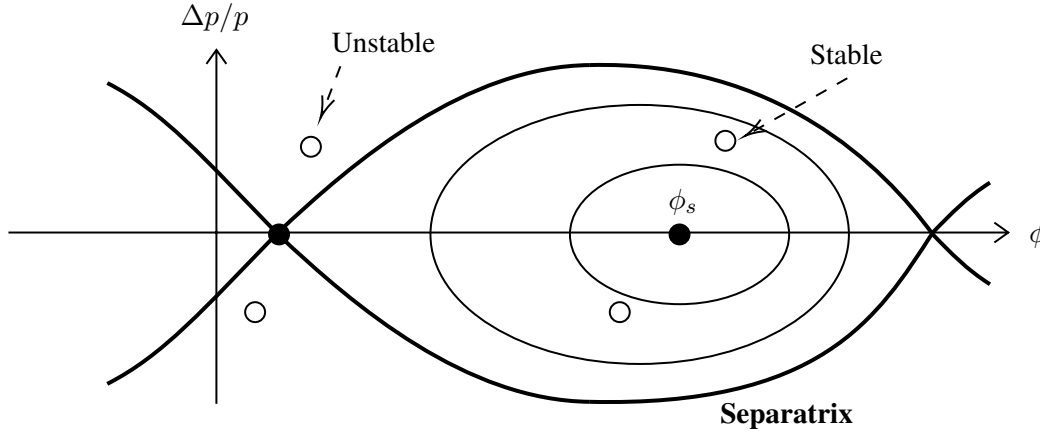


Figure 2.10: Longitudinal Phase Space, equivalent to Figure 2.9. The separatrix, bold, separates the stable and unstable regions. The four non-synchronous particles, two unstable and two stable, from Figure 2.9 are shown.

Tomography? or is that too detailed.

2.4 Slow Extraction

1. Machine resonance at third order, leading to a derivation of the Kobayashi Hamiltonian and Steinbach diagram
2. COSE (chromatic)
3. Q-sweep
4. Betatron
5. **RFKO INTRODUCE RFKO FORMALLY HERE**
6. Mathematical description of the four regimes
7. Demonstrate why RFKO is of interest
8. How i actually do RFKO at the PS - the PFW, XSE, and QSE over the cycle, the beam parameters

Chapter 3

Simulation and Benchmarking

3.1 Simulation Methodology

Focussed on original contribution

1. What tools are available? MAD-X, MapTrack, Henontrack, Xsuite
2. How do they compare? Accuracy studies between basic simulations
3. How extraction can be implemented in them: MAD-X limitation of sub-turn frequencies; Xtrack Exciter element
4. How extraction compares spill accuracy studies between simulations and machine data
5. How performance compares performance studies between SX simulations on CPU and GPGPU

Chapter 4

Conclusion

Chapter 5

Acknowledgements

Chapter 6

Bibliography

Bibliography

- [1] M. Fraser, P. A. Arrutia Sota, K. Biłko, N. Charitonidis, S. Danzeca, M. Delrieux, M. Duraffourg, N. Emriskova, L. S. Esposito, R. García Alía, A. Guerrero, O. Hans, G. Imesch, E. Johnson, G. Lerner, I. Ortega Ruiz, G. Pezzullo, D. Prelipcean, F. Ravotti, F. Roncarolo, and A. Waets, “Feasibility of Slow-Extracted High-Energy Ions From the CERN Proton Synchrotron for CHARM,” *JACoW IPAC*, vol. 2022, pp. 1703–1706, 2022. [Online]. Available: <https://cds.cern.ch/record/2845894>
- [2] M. A. Fraser, “Fast extraction: single and multi-turn,” *CERN Yellow Reports: School Proceedings*, vol. Vol 5, p. Extraction and Transfer, 2018. [Online]. Available: <https://e-publishing.cern.ch/index.php/CYRSP/article/view/703>
- [3] K. D. Metzmacher and L. Sermeus, “The PSB Ejection and Recombination Kicker Systems for LHC,” CERN, Geneva, Tech. Rep., 2000. [Online]. Available: <http://cds.cern.ch/record/2061508>
- [4] S. Ghithan, G. Roy, and S. Schuh, “Design study of beam transport lines for BioLEIR facility at CERN,” *JINST*, vol. 12, no. 09, p. P09019, 2017.
- [5] K. J. le Couteur, “The regenerative deflector for synchro-cyclotrons,” *Proceedings of the Physical Society. Section B*, vol. 64, no. 12, p. 1073, dec 1951. [Online]. Available: <https://dx.doi.org/10.1088/0370-1301/64/12/308>
- [6] —, “The extraction of the beam from the liverpool synchrocyclotron i. theoretical,” *Proceedings of the Royal Society of London. Series A. Mathematical and Physical Sciences*, vol. 232, no. 1189, pp. 236–241, oct 1955. [Online]. Available: <https://doi.org/10.1098/rspa.1955.0214>
- [7] P. A. Arrutia Sota, P. Burrows, A. De Franco, M. Fraser, B. Goddard, V. Kain, F. Kuehteubl, M. Pivi, D. Prokopovich, and F. Velotti, “Implementation of a Tune Sweep Slow Extraction with Constant Optics at MedAustron,” *JACoW IPAC*, vol. 2022, pp. 1715–1717, 2022. [Online]. Available: <https://cds.cern.ch/record/2845862>
- [8] F. C. Iselin, “THE MAD PROGRAM (METHODICAL ACCELERATOR DESIGN): REFERENCE MANUAL,” 5 1985.
- [9] H. Wiedemann, *Introduction to Accelerator Physics*. Cham: Springer International Publishing, 2015, pp. 3–41. [Online]. Available: https://doi.org/10.1007/978-3-319-18317-6_1
- [10] J. Rossbach and P. Schmüser, “Basic course on accelerator optics,” 1994. [Online]. Available: <http://cds.cern.ch/record/247501>
- [11] E. Courant and H. Snyder, “Theory of the alternating-gradient synchrotron,” *Annals of Physics*, vol. 3, no. 1, pp. 1–48, 1958. [Online]. Available: <https://www.sciencedirect.com/science/article/pii/0003491658900125>

- [12] R. D. Ruth, “An Introduction to Particle Accelerators,” *Physics Today*, vol. 55, no. 8, pp. 52–52, 08 2002. [Online]. Available: <https://doi.org/10.1063/1.1510283>
- [13] T. Mastoridis and P. Baudrenghien, “Cern’s super proton synchrotron 200 mhz cavity regulation upgrade: Modeling, design optimization, and performance estimation,” *Phys. Rev. Accel. Beams*, vol. 25, p. 021002, Feb 2022. [Online]. Available: <https://link.aps.org/doi/10.1103/PhysRevAccelBeams.25.021002>
- [14] H. Damerau and S. Hancock, “New Control Structure of the 10 MHz RF System in the CERN PS,” 2013. [Online]. Available: <https://cds.cern.ch/record/1541972>
- [15] F. Tecker, “Longitudinal Beam Dynamics in Circular Accelerators,” in *CAS - CERN Accelerator School 2019: Introduction to Accelerator Physics*, 11 2020.
- [16] H. Wiedemann, *Particle Accelerator Physics*. Springer International Publishing, 2015. [Online]. Available: <https://doi.org/10.1007/978-3-319-18317-6>
- [17] W. Hillert, “Transverse linear beam dynamics,” 2021. [Online]. Available: <https://arxiv.org/abs/2107.02614>
- [18] G. Russo, “Radio frequency knockout (rfko) extraction: Hardware analysis and beam optics simulation and optimization,” Mar 2019. [Online]. Available: <https://webthesis.biblio.polito.it/10253/>
- [19] S. Savazzi *et al.*, “Implementation of RF-KO Extraction at CNAO,” in *Proc. 10th International Particle Accelerator Conference (IPAC’19), Melbourne, Australia, 19-24 May 2019*, ser. International Particle Accelerator Conference, no. 10. Geneva, Switzerland: JACoW Publishing, Jun. 2019, paper THPMP010, pp. 3469–3471, <https://doi.org/10.18429/JACoW-IPAC2019-THPMP010>. [Online]. Available: <http://jacow.org/ipac2019/papers/thpmp010.pdf>
- [20] “Xsuite.” [Online]. Available: <xsuite.web.cern.ch>
- [21] “Cern optics repository.” [Online]. Available: <https://acc-models.web.cern.ch/acc-models/>
- [22] P. Virtanen, R. Gommers, T. E. Oliphant, M. Haberland, T. Reddy, D. Cournapeau, E. Burovski, P. Peterson, W. Weckesser, J. Bright, S. J. van der Walt, M. Brett, J. Wilson, K. J. Millman, N. Mayorov, A. R. J. Nelson, E. Jones, R. Kern, E. Larson, C. J. Carey, Í. Polat, Y. Feng, E. W. Moore, J. VanderPlas, D. Laxalde, J. Perktold, R. Cimrman, I. Henriksen, E. A. Quintero, C. R. Harris, A. M. Archibald, A. H. Ribeiro, F. Pedregosa, P. van Mulbregt, and SciPy 1.0 Contributors, “SciPy 1.0: Fundamental Algorithms for Scientific Computing in Python,” *Nature Methods*, vol. 17, pp. 261–272, 2020.
- [23] J. Duplissy, F. Hahn, U. Reichl, P. M. Winkler, E. Pedersen, V. Makhmutov, Y. Viisanen, M. Kulmala, M. Wilhelmsson, E. Weingartner, M. Avngaard, J. Curtius, R. Veenhof, L. Laakso, S. Gagne, R. G. Harrison, M. Sipila, A. David, J. H. Seinfeld, T. Nieminen, B. Verheggen, K. L. Aplin, F. Stratmann, F. Arnold, J. Makela, B. Kellett, B. Fastrup, N. D. Marsh, M. Lockwood, K. Carslaw, G. Wehrle, H. Aufmhoff, J. O. P. Pedersen, U. Baltensperger, A. Onnela, A. Laaksonen, M. B. Enghoff, J. Svensmark, H. Wex, E. Lillestol, P. E. Wagner, J. Kirkby, Y. Stozhkov, J. Polny, T. Bondo, R. Bingham, and H. Svensmark, “Results from the CERN pilot CLOUD experiment,” *Atmos. Chem. Phys.*, vol. 10, no. 4, pp. 1635–1647, 2010. [Online]. Available: <http://cds.cern.ch/record/1359385>
- [24] CERN, “Cern yellow reports: School proceedings, vol 5 (2018): Proceedings of the cas-cern accelerator school on beam injection, extraction and transfer,” 2018. [Online]. Available: <https://e-publishing.cern.ch/index.php/CYRSP/issue/view/62>
- [25] G. Russo, “Radio frequency knockout (rfko) extraction: Hardware analysis and beam optics simulation and optimization,” Mar 2019. [Online]. Available: <http://webthesis.biblio.polito.it/id/eprint/10253>

- [26] V. Nagaslaev, J. Amundson, J. Johnstone, C. Park, and S. Werkema, “Third integer resonance slow extraction using rfko at high space charge.” 2011. [Online]. Available: <https://accelconf.web.cern.ch/IPAC2011/papers/thps058.pdf>
- [27] G. Feldbauer, M. Benedikt, and U. Dorda, “Simulations of Various Driving Mechanisms for the 3rd Order Resonant Extraction from the MedAustron Medical Synchrotron,” 2011. [Online]. Available: <https://cds.cern.ch/record/1379901>
- [28] G. Sterbini, A. Blas, and S. Gilardoni, “Beam-based Performance of the CERN PS Transverse Feedback,” p. MOPAB10, 2015. [Online]. Available: <https://cds.cern.ch/record/2158994>
- [29] E. Métral, G. Arduini, F. Arnold Malandain, W. Höfle, and D. Manglunki, “Controlled Transverse Emittance Blow-up in the CERN SPS,” 2010. [Online]. Available: <https://cds.cern.ch/record/1208359>
- [30] M. Pari, F. M. Velotti, M. A. Fraser, V. Kain, and O. Michels, “Characterization of the slow extraction frequency response,” *Phys. Rev. Accel. Beams*, vol. 24, no. 8, p. 083501, 2021. [Online]. Available: <https://cds.cern.ch/record/2780495>
- [31] K. Okamura, Y. Arakaki, T. Kimura, S. Murasugi, R. Muto, Y. Shirakabe, M. Tomizawa, and E. Yanaoka, “A consideration on the transfer function between rq field and slow extraction spill in the main ring of j-parc,” *Proceedings of the 10th Int. Particle Accelerator Conf.*, vol. IPAC2019, p. Australia, 2019. [Online]. Available: <http://jacow.org/ipac2019/doi/JACoW-IPAC2019-WEPM008.html>
- [32] V. Agoritsas, “Secondary emission chambers for monitoring the CERN Proton Synchrotron ejected beams. Secondary emission chambers for monitoring the CPS ejected beams,” 1968. [Online]. Available: <https://cds.cern.ch/record/299104>
- [33] P. Actis, T. Dorenbos, and C. Johnson, “An optically coupled differential beam time structure monitor for slow extraction,” CERN, Geneva, Tech. Rep., 1976. [Online]. Available: <https://cds.cern.ch/record/2831368>
- [34] E. P. Johnson *et al.*, “Beam delivery of high-energy ion beams for irradiation experiments at the CERN Proton Synchrotron,” ser. International Particle Accelerator Conference, no. 14. JACoW Publishing, Geneva, Switzerland, paper MOPA115, presented at IPAC’23, Venice, Italy, May. 2023, paper MOPA115, this conference.
- [35] S. Deghaye, D. Jacquet, J. Kozar, and J. Serrano, “Oasis: A New System to Acquire and Display the Analog Signals for LHC,” 2003. [Online]. Available: <http://cds.cern.ch/record/693174>
- [36] M. Gasior and R. Jones, “High Sensitivity Tune Measurement by Direct Diode Detection,” 2005. [Online]. Available: <https://cds.cern.ch/record/895142>
- [37] “High throughput condor (htcondor).” [Online]. Available: <https://research.cs.wisc.edu/htcondor>
- [38] W. Hillert, “Transverse linear beam dynamics,” 2021.

Appendix A

Derivations

A.1 Relating longitudinal variables

In order to relate the dispersive and chromatic functions produced by MAD-X to those calculated by Xtrack, we must multiply MAD-X's results by the relativistic Lorentz factor $\beta = v/c$. This is because MAD-X uses the relative momentum error δ_p as a longitudinal variable, defined as

$$\delta_p = \frac{p - p_0}{p_0} \tag{Eq. A.1}$$

, where p is the momentum of the particle, and p_0 the momentum of the *reference* (or *design*) particle, whereas Xtrack uses the relative energy error

Appendix B

Code Snippets

Appendix C

Data and Plots